

Black TiO₂ Nanoparticle/Carbonized Melamine Sponge Photothermal Conversion Layers for Improved Low-Temperature Performance of Supercapacitors

Fei Yu, Jialun Li, Yi Jiang, Liying Wang, Xijia Yang, Xuesong Li,* and Wei Lü*

Cite This: *ACS Appl. Nano Mater.* 2023, 6, 13284–13290

Read Online

ACCESS |



Metrics & More



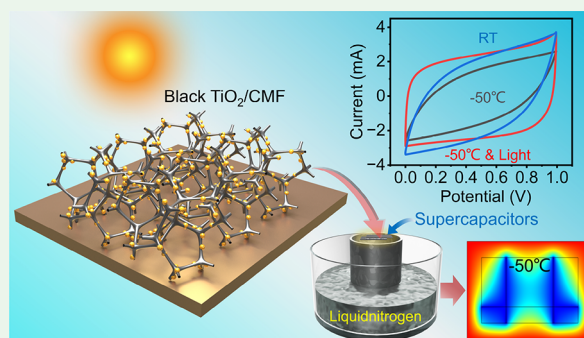
Article Recommendations



Supporting Information

ABSTRACT: Energy storage devices for example supercapacitors suffer from severe capacitance decay at low temperature, which limits their application in extreme conditions. In spite of great efforts dedicated to develop a low-temperature-resistant electrolyte, the problem is still not solved satisfactorily. In this work, to address the problem, black TiO₂/carbonized melamine sponge (CMF) was designed and prepared by adjusting the band gap of TiO₂ nanoparticles due to the excellent photothermal conversion ability of black TiO₂ nanoparticles. Benefiting from its excellent photothermal conversion ability, the performance of flexible supercapacitors at low temperatures has been greatly improved. A supercapacitor based on activated carbon electrodes is encapsulated in black TiO₂/CMF serving as a photothermal conversion layer at low temperature. The specific capacitance of a supercapacitor is improved by 287.67% at −15 °C and improved by 187.51% at −50 °C under solar illumination. The proposed photothermal conversion material in this work shows great potential under a low-temperature environment and can be extended to other energy storage devices.

KEYWORDS: *nanomaterials, photothermal conversion, black TiO₂, carbonized sponge, low-temperature resistance, supercapacitors*



1. INTRODUCTION

Efficient storage and utilization of energy are essential to alleviate energy consumption.^{1,2} Therefore, energy storage devices have been widely investigated. As a typical energy storage device, supercapacitors (SCs) have attracted great attention due to fast charging/discharging capability, high power density, and long cycle life. However, their poor performance under a low-temperature extreme environment limits their application.^{3,4} This is due to the gradual increase in the internal resistance of the electrolyte, which leads to the inactivation of the electrolyte and the decrease of the anion and cation mobility in the electrolyte.^{5–8} At present, the main strategy to address this issue is to develop a low-temperature-resistant electrolyte. Numerous electrolytes such as PVA-LiCl-glycerol,⁹ PAM-PVP GPE,¹⁰ and cross-linked PVA hydrogel¹¹ have been prepared and applied in SCs, which did improve SC performance at low temperature. In spite of great efforts dedicated to developing low-temperature-resistant electrolytes, they still suffer from low ion conductivity, complex preparation process, attenuation problems, moisture sensitivity, and limited temperature range.^{12–14}

To further boost SC performance in low-temperature environments, the idea of integrating a photothermal conversion layer composed of photothermal conversion materials to SCs has been suggested. Photothermal materials are a class of materials that convert absorbed light energy into

heat energy. Photothermal effect refers to the interaction between photon energy and lattice under illumination, which could provide local thermal energy driven to SCs at low temperature to improve the energy storage performance.¹⁵ Currently, photothermal conversion materials applied in SC are mainly carbon-based materials such as three-dimensional layered and porous graphene.^{5,16} In addition to carbon-based materials, semiconductor materials are widely used as photothermal materials too. In 2011, Chen et al. first reported the black TiO₂ produced by hydrogenation, which induced the enhanced long-wavelength absorption and conductivity in the visible and near-infrared regions.¹⁷ The extensive absorption of black TiO₂ is attributed to the introduction of oxygen vacancies, which provide more electron transport channels, capture more light energy, and reduce the TiO₂ forbidden band width through defects, thus enhancing the efficiency of light absorption over a wider wavelength range and facilitating solar absorption in the UV to IR region of the solar

Received: May 5, 2023

Accepted: July 3, 2023

Published: July 17, 2023



spectrum.^{18,19} Although most of the reports on black TiO₂ are related to photocatalysts, its wide absorption provides the possibility to be used for photothermal conversion.

Based on the aforementioned discussion, combining black TiO₂ nanoparticles with carbon-based 3D materials is expected to be an effective strategy to further improve low-temperature resistance of SCs. Herein, black TiO₂ nanoparticles with 50 nm in diameter was prepared, which is attached to a carbonized sponge skeleton (CMF) to form a black TiO₂ nanoparticle/CMF photothermal conversion layer. The photothermal conversion layer is covered on the surface of SCs to boost the low-temperature performance of SCs. Due to the better photothermal conversion ability of the black TiO₂ nanoparticle/CMF composite compared to that of pure CMF, the SC performance at low temperature is greatly enhanced. The specific capacitance of SC is improved by 287.67% at -15 °C and improved by 187.51% at -50 °C under solar illumination. The preparation process and test configuration of black TiO₂ nanoparticle/CMF are shown in Figure 1. Figure 1a–d shows

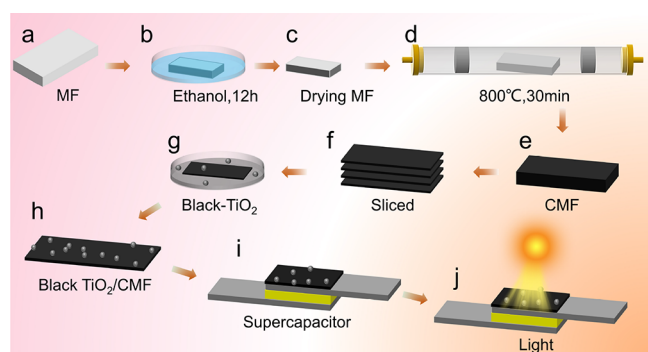


Figure 1. Schematic diagram of the preparation process of black TiO₂/CMF and test configuration of the SC working under illumination. (a–d) Treatment process of commercial melamine sponge (MF), which is washed and kept at 800 °C for 30 min under the protection of N₂ to get CMF; (e–h) the CMF is cut into slices with 1 mm in thickness and dipped into a solution of black TiO₂ nanoparticles to acquire a black TiO₂/CMF conversion layer. (i) The layer is attached on SC; (j) tested under illumination of sunlight.

the treatment process of commercial melamine sponge (MF), which is washed and kept at 800 °C for 30 min under the protection of N₂ to get CMF. As shown in Figure 1e–h, the CMF is cut into slices with 1 mm in thickness and dipped into a solution of black TiO₂ nanoparticles to acquire a black TiO₂/CMF conversion layer. The layer is attached on SC as shown in Figure 1i and tested under illumination of sunlight as shown in Figure 1j.

2. MATERIAL AND METHODS

2.1. Preparation Method of Black TiO₂ Nanoparticles. Black TiO₂ was prepared by NaBH₄ reduction method using commercial white TiO₂ as reactant. First, 4.0 g TiO₂ and 1.5 g NaBH₄ were ground in an agate mortar for 30 min to make them fully mixed. Then, it was transferred to a tube furnace, and heated at 350 °C under nitrogen protection for 2 h. The resulted black TiO₂ nanoparticles are washed and dispersed in deionized water for later use.²⁰

2.2. Preparation of CMF and Black TiO₂/CMF. At first, the commercial melamine sponge (MF) foam was cut and washed with acetone, ethanol, and deionized water each for 1 h. The MF was then dried and heated to 800 °C for 30 min in N₂ to acquire CMF. The CMF was dipped in nitric acid for 12 h and washed with deionized water, and it was further soaked in black TiO₂ solution to acquire

black TiO₂/CMF.²¹ The detailed preparation process of the organic hydrogel electrolyte, assembling SCs, and characterization are shown in the Supporting Information.

3. RESULTS AND DISCUSSION

The scanning electron microscope (SEM) images of CMF and black TiO₂/CMF at different magnifications are shown in Figure 2. As shown in Figure 2a–c, the SEM images of CMF

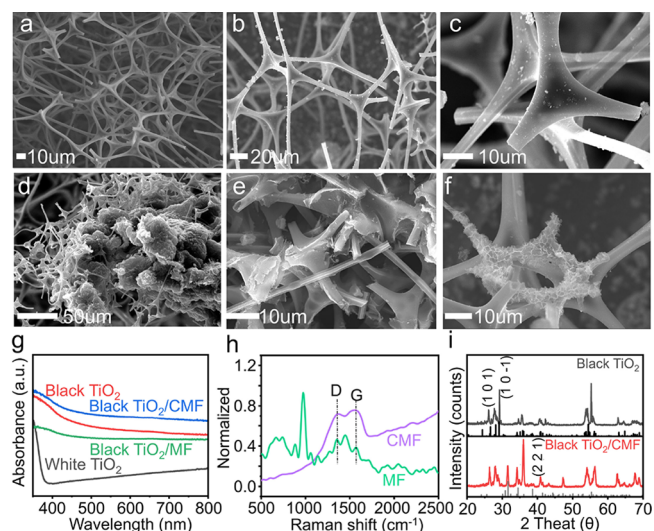


Figure 2. (a–c) SEM images of CMF; (d–f) SEM images of black TiO₂/CMF; (g) absorption spectra of white-TiO₂, black TiO₂, black TiO₂/MF, and black TiO₂/CMF; (h) Raman spectra of MF and CMF; (i) XRD curve of black TiO₂ and black TiO₂/CMF.

indicate that the CMF is a typical 3D porous structure. For black TiO₂/CMF in Figure 2d–f, it can be seen that the black TiO₂ particles are embedded in 3D CMF. The absorption spectra of white-TiO₂, black TiO₂, black TiO₂/MF, and black TiO₂/CMF are shown in Figure 2g. There is significant UV absorption exhibited by white-TiO₂, and the intensity of the absorption peak decreases rapidly after 400 nm. For black TiO₂, the absorption is enhanced compared with that of white-TiO₂, especially in the range of 400–800 nm. Further, the UV absorption spectrum of black TiO₂/CMF is higher than that of black TiO₂, which proves that the composite photothermal material black TiO₂/CMF has a higher light absorption capacity than that of black TiO₂. Black TiO₂ has a large number of defects and active sites on its surface, which provide more electron transport channels, capture more light energy, and reduce the TiO₂ forbidden band width through defects, thus enhancing the efficiency of light absorption over a wider wavelength range and facilitating solar absorption in the UV to IR region of the solar spectrum.²² However, the UV absorption spectrum of the black TiO₂/MF composite shows a much lower absorption peak than that of black TiO₂ and the black TiO₂/CMF, which is due to the low carbon content and white color of MF. The overall comparison indicates that black TiO₂/CMF has the strongest light absorption ability. Figure S1a–e is the TEM images of black TiO₂ nanoparticles under different magnifications, indicating that the average diameter of black TiO₂ nanoparticles is ~50 nm. In Figure S1e, the lattice spacing of 0.376 nm corresponds to the (1 0 1) plane of TiO₂. Figure S1f shows the elemental distribution of black TiO₂, and Ti and O elements are evenly distributed. The Raman spectra are shown in Figure 2h. The peaks at 1058 cm⁻¹ (N–N–N

ring) and 2964 cm^{-1} (C–H bond) in MF disappeared after carbonization, indicating the formation of carbon. Figure 2i is the X-ray diffraction (XRD) curve of black TiO_2 and black TiO_2/CMF . The characteristic peaks prove the existence of black TiO_2 in black TiO_2/CMF , and black TiO_2 contains oxygen vacancies.²³

The temperature variations of black TiO_2/CMF , CMF, and black TiO_2 with increasing illumination time are shown in Figure 3a. In 30 s, for black TiO_2 , the temperature increases

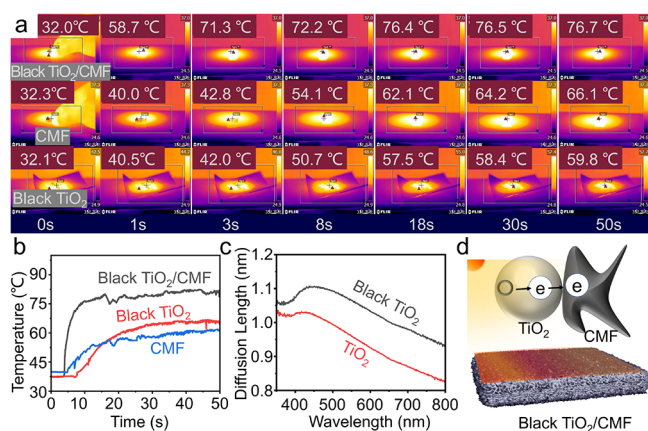


Figure 3. (a) Infrared thermographic images of the surface temperature variation of black TiO_2/CMF , CMF, and black TiO_2 with time during illumination; (b) Temperature rise curve of the surface temperature of black TiO_2/CMF , CMF, and black TiO_2 during illumination; (c) diffusion length of black TiO_2 and TiO_2 ; (d) diagram of the black TiO_2/CMF photothermal conversion mechanism.

from 32.1 to $58.4\text{ }^\circ\text{C}$, and that of CMF increases from 32.3 to $64.2\text{ }^\circ\text{C}$. For black TiO_2/CMF , the temperature increases from 32.0 to $76.5\text{ }^\circ\text{C}$ in 30 s. Figure 3b shows temperature profiles of black TiO_2/CMF , black TiO_2 , and CMF material surfaces under one sun illumination. It can be seen that the temperature rise rate and stability temperature of black TiO_2/CMF are the

highest than those of black TiO_2 and CMF, indicating that the coupling of black TiO_2 and CMF improves the photothermal conversion of the composites.²⁴ It is also able to convert photonic energy into thermal energy, thus forming a hot spot on the surface and transferring the photothermal energy to the surrounding area. In carbon materials, the presence of diverse electron orbital properties and anisotropy in sp , sp^2 , and sp^3 hybridization produces a photothermal conversion, which absorbs photons.²⁵ When the photon energy is greater than the band gap of the material, it excites electrons and holes within the material and causes them to leap into the conduction and valence bands.^{26,27} The electron–hole pairs are attracted to each other and eventually recombine, at which point the energy is released in the form of heat. This process is repeated until sufficient heat has been generated throughout the carbon material.^{17–19} Figure 3c shows the diffusion distances of carriers in white- TiO_2 and black TiO_2 . Black TiO_2 has a higher carrier diffusion length than that of white- TiO_2 . Materials with longer carrier diffusion lengths can make better utilization of light energy, thus increasing the photothermal conversion efficiency. In semiconductor materials, longer carrier diffusion distances increase the carrier relaxation time at the material surface and can improve the photothermal conversion efficiency. Figure 3d shows the contact between black TiO_2 and CMF under illumination. When electrons are excited from the valence band (VB) to the conduction band (CB) in black TiO_2 , charge vacancies or holes (h^+) in the VB are created. In the case of the absence of CMF, most of these charges recombine rapidly. When the CMF is attached to the surface of black TiO_2 , the relative positions of the CMF conduction band edges allow electron transfer from the black TiO_2 surface, resulting in charge separation and hindering recombination, thereby generating thermal energy.²⁰

In order to explore the excellent photothermal conversion ability of TiO_2 nanoparticles containing oxygen vacancies, we use the first principles to calculate the energy band structure and density of states (DOS) of anatase TiO_2 , black anatase TiO_2 , rutile TiO_2 , and black rutile TiO_2 . The unit cell

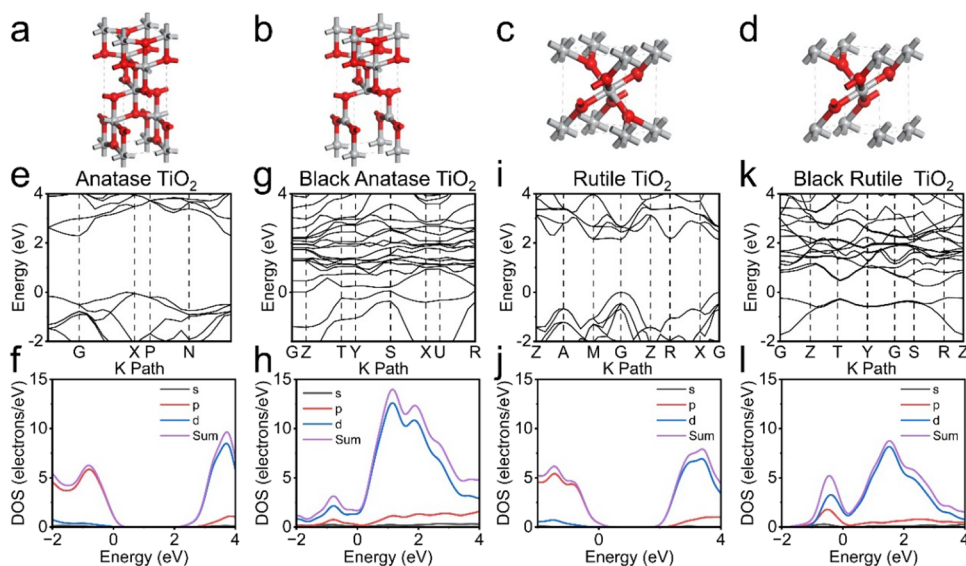


Figure 4. (a) Unit cell structure of anatase TiO_2 ; (b) unit cell structure of black anatase TiO_2 ; (c) unit cell structure of rutile TiO_2 ; (d) unit cell structure of black rutile TiO_2 ; (e, f) band structure and DOS of anatase TiO_2 ; (g, h) band structure and DOS of black anatase TiO_2 ; (i, j) band structure and DOS of rutile TiO_2 ; (k, l) band structure and DOS of black rutile TiO_2 .

structures of the four materials are shown in Figure 4a–d. Figure 4e,f are the band structure and DOS of anatase TiO₂; the calculation results show that the band gap of TiO₂ without defects is about 3.291 eV, and the experimental value is 3.2 eV.²⁸ Figure 4g,h shows the band structure and DOS of black anatase TiO₂, and the band gap according to theoretical calculation is reduced to 1.242 eV. For rutile TiO₂, the calculated band gap is 3.130 eV as shown in Figure 4i,j. Also, the band gap of black rutile TiO₂ is reduced to 1.471 eV as shown in Figure 4k,l. Previous investigations have indicated that the changed properties of black TiO₂ are due to the introduction of oxygen vacancies. Oxygen vacancies can capture the surrounding electrons to form a localized state, resulting in changes in the energy level of the electrons, inducing in an increase in the density of electrons and holes near the band gap, thereby reducing the band gap.^{29–31} It can be seen from Figure S2, that the theoretical light absorption ability of black anatase TiO₂ and black rutile TiO₂ containing defects is higher than that of anatase TiO₂ and rutile TiO₂.^{32,33} When the band gap of TiO₂ is reduced, lower-energy photons can be absorbed, allowing TiO₂ to absorb visible and near-ultraviolet light more efficiently.

Figure 5 is the simulation of the temperature field distribution of CMF and black TiO₂/CMF under illumination.

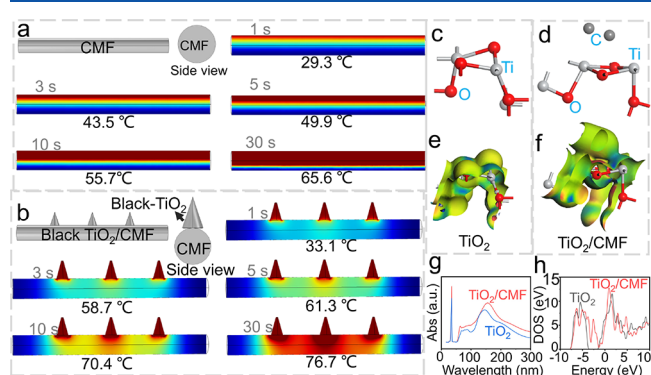


Figure 5. (a) Temperature field distribution of CMF under illumination; (b) temperature field distribution of black TiO₂/CMF under illumination; (c) TiO₂ (1 0 1) crystalline structure; (d) TiO₂(101)/CMF molecular structure; (e) TiO₂ differential charge density; (f) TiO₂(101)/CMF differential charge density; (g) TiO₂ and TiO₂(101)/CMF absorption spectra calculated by first-principles calculations; (h) density of states of TiO₂ and TiO₂(101)/CMF.

The high-temperature zone is indicated by red, and the low-temperature zone is indicated by blue. The average temperatures of CMF in Figure 5a increases from 29.3 to 65.6 °C in 30 s. The temperature of the CMF surface shifted uniformly from top to bottom with a gentle temperature line. In Figure 5b, the average temperatures of black TiO₂/CMF increases from 33.1 to 76.7 °C in 30 s. From the simulation results, it can be seen that the temperature of black TiO₂/CMF rises rapidly after exposing to sunlight. The simulation results are consistent well with that of experiments. Figure 5c,d shows the crystal lattice structure of TiO₂(101) and TiO₂(101)/CMF. Figure 5e,f is the differential charge densities of TiO₂(101) and TiO₂(101)/CMF, which clearly shows that the C atom interacts with the Ti atom electron cloud when the C atom contacts with the TiO₂ interface.^{34–36} Figure 5g,h shows the absorption spectra and density of states of TiO₂ and TiO₂/CMF acquired from theoretical calculations, and it can be seen

that the light absorption ability of the TiO₂/CMF composite is enhanced. The density of states shows that the overall electron orbitals of the TiO₂/CMF material have changed and an intermediate band gap appears in the TiO₂ forbidden band region, which is beneficial to the absorption of photons and the leap of electrons at the interface between TiO₂ and CMF when TiO₂/CMF is illuminated.³⁷

Figure 6a is a schematic illustration of photothermal layer-integrated SC, and the optical images of the SC with a photothermal conversion layer under test conditions are shown in Figure S3. Figure 6b is a schematic diagram of the cryogenic tank providing a −50 °C low-temperature environment for the SCs. The bottom of the tank is injected with liquid nitrogen, and the SCs fixed at the top of the iron cylinder can reach −50 °C upon cooling. In order to simulate and verify the temperature field, the model in Figure S4 is used,^{38,39} and the calculation results are shown in Figure 6c and Figure S5. After injecting liquid nitrogen, the temperature decreases along the wall of the iron cylinder to form a local low temperature zone.⁴⁰ Figure 6d is the temperature curves corresponding to different heights of the iron cylinder, and the average temperature on the top of the cylinder is lower than −50 °C with enough cooling time, which meets the experimental requirements. Figure 6e is the GCD curves of SCs measured at RT with intermittent illumination, and the illumination is shut down during 25–50s; it can be seen that with illumination, the GCD cycle increases significantly from 9.4 s to 32 s, which is due to the photothermal effect on the surface of SC. Figure 6f shows the GCD curves with intermittent illumination at −50 °C as a function of time. Without illumination during 113–130 s, the GCD curve is shortened obviously, which is due to the fast discharge at low temperature.^{41,42} These results indicate that the photothermal effect could efficiently improve SC performance at low temperature.

According to the theoretical calculation in Figure S5, it is found that the resistance of the electrolyte decreases with increasing temperature and the ionic mobility in the electrolyte increases.^{43,44} The resistance value of electrolyte is related to the performance of SCs. The smaller resistance value of the electrolyte corresponds to a higher temperature and a larger area of CV curve.^{45–49} According to the formula for calculating the capacitance of SCs, it is found that the larger the CV area is, the greater the capacitance is.^{50–52} As shown in Figure S6, the smaller resistance of the electrolyte corresponds to a higher temperature and larger area of CV curve. Figure S7 shows the discharge curve obtained by theoretical calculations, proving that higher temperature induces lower resistance, higher capacitance, and the longer discharge time. Figure 7a,b shows the CV and GCD curves of SC measured at −20, 0, and 20 °C, respectively. The experimental results confirm that the higher temperature induces larger CV curve area and longer discharge time. These results are consistent with the results of theoretical calculations. In Figure 7c–e, the SC exhibits the smallest CV area, the shortest discharge time, and the highest resistance value at −15 °C due to the low temperature effect. By adding a black TiO₂/CMF photothermal layer on the surface of SCs, it can be observed that the CV curve area and discharge time increases, and the resistance value of the Nyquist curve decreases. This is because black TiO₂/CMF undergoes photothermal conversion after being irradiated with light, and the generated heat energy increases the temperature of SCs, thereby improving the electrochemical performance of SCs. Figure 7f–h and Figure 7i–k show the CV,

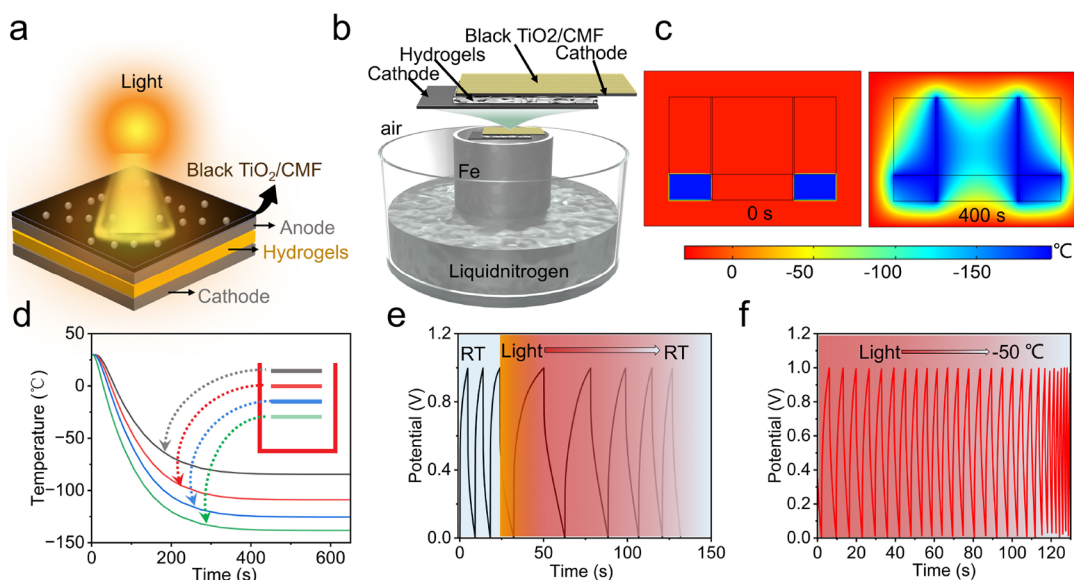


Figure 6. (a) Schematic illustration of photothermal layer integrated SCs; (b) schematic illustration of the test environment of photothermal SCs at $-50\text{ }^{\circ}\text{C}$; (c) simulation of temperature variation with time; (d) temperature curves corresponding to different heights of the iron cylinder; (e) GCD curves of SCs measured at RT with intermittent illumination, and the illumination is shut down during 25–50s; (f) GCD curves of SCs measured at $-50\text{ }^{\circ}\text{C}$ with intermittent illumination. Before 113 s, the SC is illuminated; after 113 s, the light source is shut down.

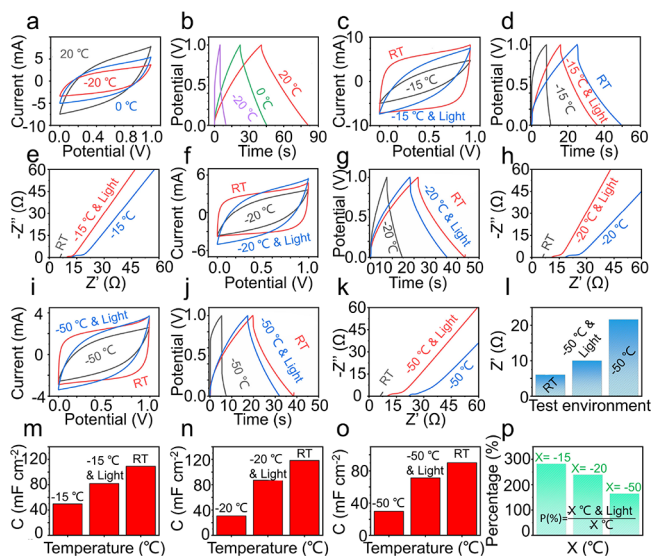


Figure 7. (a) CV curves of SCs at -20 , 0 , and $20\text{ }^{\circ}\text{C}$; (b) GCD curves of SCs at -20 , 0 , and $20\text{ }^{\circ}\text{C}$; (c–k) CV, GCD, and Nyquist curves of SC measured at different temperatures; (l) resistances of SCs in different environments; (m–o) specific capacity of SCs measured at different temperatures; (p) SCs enhance multiples over capacitors at low light temperatures.

GCD, and Nyquist curves of SCs with the black TiO_2/CMF photothermal layer under light irradiation measured at -20 and $-50\text{ }^{\circ}\text{C}$, respectively. The results indicate that the electrochemical and energy storage performance of black TiO_2/CMF combined SC can be significantly improved by light irradiation in low-temperature environments. Figure 7k shows the Nyquist curves of SCs at $-50\text{ }^{\circ}\text{C}$ without illumination, $-50\text{ }^{\circ}\text{C}$ with illumination, and RT, respectively. For SCs measured at $-50\text{ }^{\circ}\text{C}$ without illumination, it shows the largest resistance. The resistance decrease under illumination, indicating that the resistance of the electrolyte decreases with the increase of temperature, which is consistent

with the theoretical calculation in Figures S6 and S7. Figure S8 shows the discharge curve obtained by theoretical calculations, proving that higher temperature induces lower resistance, higher capacitance, and longer discharge time. Figure 7m–o shows the specific capacitance of SCs at different test environments, which is increased to after adding a black TiO_2/CMF photothermal layer under irradiation. As shown in Figure 7p, it is shown that under illumination, the specific capacitance of SCs increased by 287.67% at $-15\text{ }^{\circ}\text{C}$ and 234.15 and 187.51% at -20 and $-50\text{ }^{\circ}\text{C}$, respectively. These results indicate that present photothermal conversion material is also suitable for other energy storage devices working in low-temperature environments.

4. CONCLUSIONS

In conclusion, we propose a strategy of integrating a photothermal conversion layer to boost the low temperature performance of energy storage devices. We have developed a black TiO_2 nanoparticle/CMF composite with wide spectrum absorption and high photothermal conversion performance by combining the carbon-based skeleton's broad spectral absorption characteristics with the light absorption of black TiO_2 nanoparticles. For an all solid SC combined present photothermal conversion layer, under illumination, the specific capacitance of SC is enhanced by 287.67% at $-15\text{ }^{\circ}\text{C}$, 234.15% at $-20\text{ }^{\circ}\text{C}$, and 187.51% at $-50\text{ }^{\circ}\text{C}$. Our research has demonstrated that this innovative photothermal conversion material has enormous potential for improving the performance of other energy storage devices in low-temperature environments.

■ ASSOCIATED CONTENT

Supporting Information

The Supporting Information is available free of charge at <https://pubs.acs.org/doi/10.1021/acsnm.3c01991>.

Experimental details; TEM images of black TiO_2 nanoparticles; theoretical absorption spectrum of

anatase TiO₂, black anatase TiO₂, rutile TiO₂, and black rutile TiO₂; optical photo and infrared image of the SC device in liquid nitrogen cooling tank; model diagram of the liquid nitrogen cooling tank; one simulation of temperature variation with time; CV curves of SC with different electrolyte resistances acquired by theoretical calculation; and discharge curves acquired by theoretical calculation (PDF)

AUTHOR INFORMATION

Corresponding Authors

Xuesong Li – Key Laboratory of Advanced Structural Materials, Ministry of Education & Advanced Institute of Materials Science, Changchun University of Technology, Changchun 130012, People's Republic of China; Email: lixuesong@ccut.edu.cn

Wei Lü – Key Laboratory of Advanced Structural Materials, Ministry of Education & Advanced Institute of Materials Science, Changchun University of Technology, Changchun 130012, People's Republic of China; State Key Laboratory of Luminescence and Applications, Changchun Institute of Optics, Fine Mechanics and Physics, Chinese Academy of Sciences, Changchun 130033, People's Republic of China; orcid.org/0000-0002-7070-8456; Email: lw771119@hotmail.com

Authors

Fei Yu – Key Laboratory of Advanced Structural Materials, Ministry of Education & Advanced Institute of Materials Science, Changchun University of Technology, Changchun 130012, People's Republic of China

Jialun Li – Key Laboratory of Advanced Structural Materials, Ministry of Education & Advanced Institute of Materials Science, Changchun University of Technology, Changchun 130012, People's Republic of China

Yi Jiang – School of Science, Changchun Institute of Technology, Changchun 130012, China; orcid.org/0000-0003-3401-6986

Liyang Wang – Key Laboratory of Advanced Structural Materials, Ministry of Education & Advanced Institute of Materials Science, Changchun University of Technology, Changchun 130012, People's Republic of China

Xijia Yang – Key Laboratory of Advanced Structural Materials, Ministry of Education & Advanced Institute of Materials Science, Changchun University of Technology, Changchun 130012, People's Republic of China; orcid.org/0000-0001-9424-3596

Complete contact information is available at: <https://pubs.acs.org/10.1021/acsnm.3c01991>

Author Contributions

The manuscript was written through contributions of all authors.

Funding

This work was financially supported by the National Natural Science Foundation of China (nos. 62004015 and 62004014) and the Department of Science and Technology of Jilin Province (20210101077JC).

Notes

The authors declare no competing financial interest.

REFERENCES

- (1) Yang, T.; Liu, H.-j.; Bai, F.; Wang, E.-h.; Chen, J.-h.; Chou, K.-C.; Hou, X.-m. Supercapacitor electrode based on few layer h BNNs/rGO composite for wide temperature range operation with robust stable cycling performance. *Int. J. Miner., Metall. Mater.* **2020**, *27*, 220–231.
- (2) Liu, S.; Wang, E.; Liu, S.; Guo, C.; Wang, H.; Yang, T.; Hou, X. Mild fabrication of SiC/C nanosheets with prolonged cycling stability as supercapacitor. *J. Mater. Sci. Technol.* **2021**, *110*, 178–186.
- (3) Yu, F.; Li, J.; Jiang, Y.; Wang, L.; Yang, X.; Li, X.; Lü, W.; Sun, X. Boosting Low-Temperature Resistance of Energy Storage Devices by Photothermal Conversion Effects. *ACS Appl. Mater. Interfaces* **2022**, *14*, 23400–23407.
- (4) Ye, L.; Liang, Q.; Huang, Z. H.; Lei, Y.; Zhan, C.; Bai, Y.; Li, H.; Kang, F.; Yang, Q. H. A supercapacitor constructed with a partially graphitized porous carbon and its performance over a wide working temperature range. *J. Mater. Chem. A* **2015**, *3*, 18860–18866.
- (5) Yi, F.; Ren, H.; Dai, K.; Wang, X.; Han, Y.; Wang, K.; Li, K.; Guan, B.; Wang, J.; Tang, M.; Shan, J.; Yang, H.; Zheng, M.; You, Z.; Wei, D.; Liu, Z. Solar thermal driven capacitance enhancement of supercapacitors. *Energy Environ. Sci.* **2018**, *11*, 2016–2024.
- (6) Xu, J.; Wang, X.; Zhou, X.; Yuan, N.; Ge, S.; Ding, J. Activated carbon coated CNT core-shell nanocomposite for supercapacitor electrode with excellent rate performance at low temperature. *Electrochim. Acta* **2019**, *301*, 478–486.
- (7) Xu, J.; Yuan, N.; Razal, J. M.; Zheng, Y.; Zhou, X.; Ding, J.; Cho, K.; Ge, S.; Zhang, R.; Gogotsi, Y.; Baughman, R. H. Temperature independent capacitance of carbon based supercapacitor from –100 to 60 °C. *Energy Storage Mater.* **2019**, *22*, 323–329.
- (8) Xu, S. W.; Zhang, M. C.; Zhang, G. Q.; Liu, J. H.; Liu, X. Z.; Zhang, X.; Zhao, D. D.; Xu, C. L.; Zhao, Y. Q. Temperature-dependent performance of carbon-based supercapacitors with water-in-salt electrolyte. *J. Power Sources* **2019**, *441*, No. 227220.
- (9) Hou, X.; Zhang, Q.; Wang, L.; Gao, G.; Lü, W. Low-Temperature-Resistant Flexible Solid Supercapacitors Based on Organohydrogel Electrolytes and Microvoid-Incorporated Reduced Graphene Oxide Electrodes. *ACS Appl. Mater. Interfaces* **2021**, *13*, 12432–12441.
- (10) Wang, M.; Fan, L.; Qin, G.; Hu, X.; Wang, Y.; Wang, C.; Yang, J.; Chen, Q. Flexible and low temperature resistant semi-IPN network gel polymer electrolyte membrane and its application in supercapacitor. *J. Membr. Sci.* **2020**, *597*, No. 117740.
- (11) Liu, Z.; Zhang, J.; Liu, J.; Long, Y.; Fang, L.; Wang, Q.; Liu, T. Highly compressible and superior low temperature tolerant supercapacitors based on dual chemically crosslinked PVA hydrogel electrolytes. *J. Mater. Chem. A* **2020**, *8*, 6219–6228.
- (12) Przygocki, P.; Abbas, Q.; Gorska, B.; Béguin, F. High-energy hybrid electrochemical capacitor operating down to –40 °C with aqueous redox electrolyte based on choline salts. *J. Power Sources* **2019**, *427*, 283–292.
- (13) Zheng, T.; Xiong, J.; Zhu, B.; Shi, X.; Cheng, Y. J.; Zhao, H.; Xia, Y. From –20 °C to 150 °C: a lithium secondary battery with a wide temperature window obtained via manipulated competitive decomposition in electrolyte solution. *J. Mater. Chem. A* **2021**, *9*, 9307–9318.
- (14) Zhou, Y.; Ghaffari, M.; Lin, M.; Xu, H.; Xie, H.; Koo, C. M.; Zhang, Q. M. High performance supercapacitor under extremely low environmental temperature. *RSC Adv.* **2015**, *5*, 71699–71703.
- (15) Fan, R.; Zheng, N.; Sun, Z. Enhanced photothermal conversion capability of melamine foam-derived carbon foam-based form-stable phase change composites. *Energy Convers. Manage.* **2022**, *263*, No. 115693.
- (16) Xu, Y.; Zhu, L.; Cui, X.; Zhao, M.; Li, Y.; Chen, L.; Jiang, W.; Jiang, T.; Yang, S.; Wang, Y. Graphitizing N doped mesoporous carbon nanospheres via facile single atom iron growth for highly efficient oxygen reduction reaction. *Nano Res.* **2020**, *13*, 752–758.
- (17) Chen, X.; Liu, L.; Yu, P. Y.; Mao, S. S. Increasing solar absorption for photocatalysis with black hydrogenated titanium dioxide nanocrystals. *Science* **2011**, *331*, 746–750.

- (18) Mu, X.; Wang, J.; Sun, M. Visualization of Photoinduced Charge Transfer and Electron–Hole Coherence in Two-Photon Absorption. *J. Phys. Chem. C* **2019**, *123*, 14132–14143.
- (19) Tiene, A.; Levensen, J.; Parish, M. M.; MacDonald, A. H.; Keeling, J.; Marchetti, F. M. Extremely imbalanced two-dimensional electron-hole-photon systems. *Phys. Rev. Res.* **2020**, *2*, No. 023089.
- (20) Wang, M.; Deng, K.; Lü, W.; Deng, X.; Li, K.; Shi, Y.; Ding, B.; Cheng, Z.; Xing, B.; Han, G.; Hou, Z.; Lin, J. Rational Design of Multifunctional Fe@ γ -Fe₂O₃@H-TiO₂ Nanocomposites with Enhanced Magnetic and Photoconversion Effects for Wide Applications: From Photocatalysis to Imaging-Guided Photothermal Cancer Therapy. *Adv. Mater.* **2018**, *30*, No. 1706747.
- (21) Kuo, W. S.; Wu, C. M.; Yang, Z. S.; Chen, S. Y.; Chen, C. Y.; Huang, C. C.; Li, W. M.; Sun, C. K.; Yeh, C. S. Biocompatible bacteria@Au composites for application in the photothermal destruction of cancer cells. *Chem. Commun.* **2008**, 4430–4432.
- (22) Meng, D.; Yang, S.; Guo, L.; Li, G.; Ge, J.; Huang, Y.; Bielawski, C. W.; Geng, J. The enhanced photothermal effect of graphene/conjugated polymer composites: photoinduced energy transfer and applications in photocontrolled switches. *Chem. Commun.* **2014**, *50*, 14345–14348.
- (23) Liu, Y.; Tian, L.; Tan, X.; Li, X.; Chen, X. Synthesis, properties, and applications of black titanium dioxide nanomaterials. *Sci. Bull.* **2017**, *62*, 431–441.
- (24) Xiao, L.; Chen, X.; Yang, X.; Sun, J.; Geng, J. Recent Advances in Polymer Based Photothermal Materials for Biological Applications. *ACS Appl. Polym. Mater.* **2020**, *2*, 4273–4288.
- (25) Wang, X.; Dai, L.; Jiao, N.; Tung, S.; Liu, L. Superhydrophobic photothermal graphene composites and their functional applications in microrobots swimming at the air/water interface. *Chem. Eng. J.* **2021**, *422*, No. 129394.
- (26) Bertuccio, G.; Maiocchi, D. Electron hole pair generation energy in gallium arsenide by α and γ photons. *J. Appl. Phys.* **2002**, *92*, 1248–1255.
- (27) Gao, F.; Campbell, L. W.; Xie, Y.; Devanathan, R.; Peurrung, A. J.; Weber, W. J. Electron Hole Pairs Created by Photons and Intrinsic Properties in Detector Materials. *IEEE Trans. Nucl. Sci.* **2008**, *55*, 1079–1085.
- (28) Bo, Z.; Cuixing, L.; Jun, Z.; Yanjun, H.; Bin, L. First-principles calculations of the electronic and optical properties of carbon doped anatase titanium dioxide. *J. Sichuan Univ.* **2011**, *48*, 389–394.
- (29) Fu, W.; Zhao, E.; Ma, R.; Sun, Z.; Yang, Y.; Sevilla, M.; Furtés, A. B.; Magasinski, A.; Yushin, G. Anatase TiO₂ Confined in Carbon Nanopores for High-Energy Li-Ion Hybrid Supercapacitors Operating at High Rates and Subzero Temperatures. *Adv. Energy Mater.* **2020**, *10*, 1902993.
- (30) Liu, Q.; Zhou, J.; Song, C.; Li, X.; Wang, Z.; Yang, J.; Cheng, J.; Li, H.; Wang, B. 2.2V high performance symmetrical fiber-shaped aqueous supercapacitors enabled by “water-in-salt” gel electrolyte and N-Doped graphene fiber. *Energy Storage Mater.* **2020**, *24*, 495–503.
- (31) Lu, N.; Na, R.; Li, L.; Zhang, C.; Chen, Z.; Zhang, S.; Luan, J.; Wang, G. Rational Design of Antifreezing Organohydrogel Electrolytes for Flexible Supercapacitors. *ACS Appl. Energy Mater.* **2020**, *3*, 1944–1951.
- (32) Bi, D.; Li, Y.; Yao, Y.; Tao, T.; Liang, B.; Lu, S. Preparation and characterizations of flexible photothermal Ti₂O₃-PVA nanocomposites. *J. Alloys Compd.* **2020**, *825*, No. 153998.
- (33) Xi, S.; Wang, M.; Wang, L.; Xie, H.; Yu, W. 3D reduced graphene oxide aerogel supported TiO_{2-x} for shape-stable phase change composites with high photothermal efficiency and thermal conductivity. *Sol. Energy Mater. Sol. Cells* **2021**, *226*, No. 111068.
- (34) Ha, J. U.; Lee, J.; Abbas, M. A.; Lee, M. D.; Lee, J.; Bang, J. H. Designing Hierarchical Assembly of Carbon-Coated TiO₂ Nanocrystals and Unraveling the Role of TiO₂/Carbon Interface in Lithium-Ion Storage in TiO₂. *ACS Appl. Mater. Interfaces* **2019**, *11*, 11391–11402.
- (35) Zhang, R.; Santangelo, S.; Fazio, E.; Neri, F.; D’Arienzo, M.; Morazzoni, F.; Zhang, Y.; Pinna, N.; Russo, P. A. Stabilization of Titanium Dioxide Nanoparticles at the Surface of Carbon Nanomaterials Promoted by Microwave Heating. *Chem. - Eur. J.* **2015**, *12*, 14901–14910.
- (36) Tulus; Marpaung, T. J.; Siringoringo, Y. B.; Syahputra, M. R.; Suriati. Heat transfer simulation on window glass using COMSOL multiphysic. *J. Phys.: Conf. Ser.* **2019**, *1235*, No. 012065.
- (37) Yamaguchi, M.; Kamide, K.; Ogawa, T.; Yamamoto, Y. BEC–BCS laser crossover in Coulomb-correlated electron–hole–photon systems. *New J. Phys.* **2012**, *14*, No. 065001.
- (38) Gao, X.; Du, X.; Mathis, T. S.; Zhang, M.; Wang, X.; Shui, J.; Gogotsi, Y.; Xu, M. Maximizing ion accessibility in MXene-knotted carbon nanotube composite electrodes for high-rate electrochemical energy storage. *Nat. Commun.* **2020**, *11*, 6160.
- (39) Liu, Y.; Yu, S.; Feng, R.; Bernard, A.; Liu, Y.; Zhang, Y.; Duan, H.; Shang, W.; Tao, P.; Song, C.; Deng, T. A bioinspired, reusable, paper-based system for high-performance large-scale evaporation. *Adv. Mater.* **2015**, *27*, 2768–2774.
- (40) Wang, Z.; Liu, Y.; Tao, P.; Shen, Q.; Yi, N.; Zhang, F.; Liu, Q.; Song, C.; Zhang, D.; Shang, W.; Deng, T. Bio-inspired evaporation through plasmonic film of nanoparticles at the air–water interface. *Small* **2014**, *10*, 3234–3239.
- (41) Mathis, T. S.; Kurra, N.; Wang, X.; Pinto, D.; Simon, P.; Gogotsi, Y. Energy Storage Data Reporting in Perspective—Guidelines for Interpreting the Performance of Electrochemical Energy Storage Systems. *Adv. Energy Mater.* **2019**, *9*, 1902007.
- (42) Peng, S.; Jiang, X.; Xiang, X.; Chen, K.; Chen, G.; Jiang, X.; Hou, L. High-performance and flexible solid-state supercapacitors based on high toughness and thermoplastic poly(vinyl alcohol)/NaCl/glycerol supramolecular gel polymer electrolyte. *Electrochim. Acta* **2019**, *324*, No. 134874.
- (43) Asbani, B.; Douard, C.; Brousse, T.; Le Bideau, J. High temperature solid-state supercapacitor designed with ionogel electrolyte. *Energy Storage Mater.* **2019**, *21*, 439–445.
- (44) Wu, W.; Wang, E.-H.; Yang, T.; Hou, X.-m. Electrochemical performance of self-assembled two-dimensional Ti₃C₂T_x(MXene) thin films. *Chin. J. Eng.* **2021**, *43*, 808–815.
- (45) Bhat, M. Y.; Yadav, N.; Hashmi, S. A. Pinecone-derived porous activated carbon for high performance all-solid-state electrical double layer capacitors fabricated with flexible gel polymer electrolytes. *Electrochim. Acta* **2019**, *304*, 94–108.
- (46) Cai, J.; Wang, Y.; Qiao, X.; Zhou, X.; Mansour, A. N. A novel mediator-containing polyvinylidene fluoride/lithium trifluoromethanesulfonate polymer electrolyte membrane for low-temperature solid-state supercapacitors. *Mater. Lett.* **2019**, *251*, 26–29.
- (47) Chaichi, A.; Venugopalan, G.; Devireddy, R.; Arges, C.; Gartia, M. R. A Solid-State and Flexible Supercapacitor That Operates across a Wide Temperature Range. *ACS Appl. Energy Mater.* **2020**, *3*, 5693–5704.
- (48) Zhang, X.; Wang, Y.; Gai, Z.; Zhang, M.; Liu, S.; Guo, F.; Yang, N.; Jiang, X. Synthesis of graphene interlayer diamond films for enhanced electrochemical performance. *Carbon* **2022**, *196*, 602–611.
- (49) Diao, W.; Wu, L.; Ma, X.; Wang, L.; Bu, X.; Ni, W.; Yang, X.; Fang, Y. Reversibly highly stretchable and self-healable zwitterion-containing polyelectrolyte hydrogel with high ionic conductivity for high-performance flexible and cold-resistant supercapacitor. *J. Appl. Polym. Sci.* **2020**, *137*, 48995.
- (50) Brandon, E. J.; West, W. C.; Smart, M. C.; Whitcanack, L. D.; Plett, G. A. Extending the low temperature operational limit of double layer capacitors. *J. Power Sources* **2007**, *170*, 225–232.
- (51) Borges, R. S.; Reddy, A. L. M.; Rodrigues, M.-T. F.; Gullapalli, H.; Balakrishnan, K.; Silva, G. G.; Ajayan, P. M. Supercapacitor operating at 200 degrees celsius. *Sci. Rep.* **2013**, *3*, 2572.
- (52) Bu, X.; Zhang, Y.; Sun, Y.; Su, L.; Meng, J.; Lu, X.; Yan, X. All-climate aqueous supercapacitor enabled by a deep eutectic solvent electrolyte based on salt hydrate. *J. Energy Chem.* **2020**, *49*, 198–204.